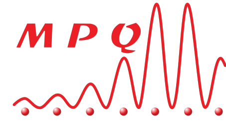

Politecnico di Torino - Université Paris Cité

Lab: Matériaux et Phénomènes Quantiques (MPQ)

Group: Dispositifs Optiques Non-linéaires (DON)

Development of metalenses for the visible and near-infrared spectral ranges

Master Degree Thesis

M2 - Quantum Devices
Double Degree Program NanoQuad

Candidate:
Martina EVANGELISTA

Supervisor:
Prof. Giuseppe LEO

Paris, June 2024

Summary

Metalenses have emerged as a highly promising technology in the field of optics. They consist of minute structures organized on a substrate in two-dimensional arrays of subwavelength-spaced optical scatterers. Unlike the bulky nature of conventional lenses, metalenses feature a flat, lightweight design while delivering superior performance. By controlling light at the nanoscale, they enable extraordinary manipulation of light waves, offering benefits such as aberration correction, customized wavefront shaping, and improved focusing abilities. The DON team at the MPQ laboratory, where I completed my master's internship, focuses on metalenses as one of their main research areas.

The primary objective of my work was to fabricate metalenses using amorphous titanium dioxide (TiO_2) for visible wavelengths and amorphous silicon (a-Si) for near-infrared (NIR) applications.
This report outlines the critical steps in the fabrication process, highlighting essential technological techniques such as Atomic Layer Deposition (ALD) and Reactive Ion Etching (RIE). The aim is to provide a comprehensive examination of these processes and their roles in achieving the desired optical properties.

Contents

1 Introduction **1**

2 Theoretical Background **2**
2.1 Metasurfaces . . . 2
2.2 Optical Metalenses . . . 3
2.3 State of art . . . 4

3 Nanofabrication **6**
3.1 TiO_2 Metalenses Fabrication . . . 6
3.1.1 Cleaning . . . 7
3.1.2 Spin Coating . . . 7
3.1.3 Electron Beam Lithography . . . 9
3.1.4 Development . . . 10
3.1.5 Atomic Layer Deposition . . . 10
3.1.6 Reactive Ion Etching . . . 16
3.2 a-Si Metalenses Fabrication . . . 19
3.2.1 Cleaning . . . 20
3.2.2 Spin Coating . . . 20
3.2.3 Electron Beam Lithography . . . 20
3.2.4 Development . . . 20
3.2.5 Metal deposition . . . 20
3.2.6 Lift-Off . . . 21
3.2.7 Reactive Ion Etching . . . 21
3.2.8 Nickel removal . . . 25

4 Experimental Set-up **26**

5 Conclusions and Outlook **28**

List of Figures

2.1 (a) Nano-fins used for geometrical phase, (b) Nano-rods used as truncated waveguides and (c) Nano-disks used for Huygens metalens. [6]. 3
2.2 Operating mechanisms of refractive lens and metalens [7]. 3
2.3 Top-view of a substrate-free a-Si nanodisk array on the c-Si surface. 4
2.4 Harvard protocol for TiO_2 metalenses [1]. 5
(a) Fabrication process. 5
(b) Scanning electron microscope image of fabricated structures - large-scale view of a fabricated metasurface hologram composed of TiO_2 nanofins. 5

3.1 Fabrication steps for a TiO_2 metasurface. 7
3.2 Spin curve of AR-P 6200.13. 8
3.3 Example of well-developed and fully exposed resist versus incompletely developed resist due to insufficient exposure. 10
3.4 Atomic Layer Deposition Process [12]. 11
3.5 XRD analysis on sample 002 - peaks originate from the silicon substrate. . 13
3.6 Real and imaginary part of the refractive index n+ik, as measured on the TiO_2 films fabricated according to our recipes. 14
(a) Real part of refractive index. 14
(b) Imaginary part of refractive index. 14
3.7 DOE BoxPlot for TiO_2 tests. Temperature and H_2O purge time are the parameters that most significantly influence the final thickness. 15
3.8 Measured real and imaginary part of the complex refractive index as a function of wavelength. 16
3.9 Interferometric signal highlighting the transition between TiO_2 and AR-P 6200.13. 17
3.10 SEM observation of the final sample. 17
3.11 SEM imaging of the final sample, highlighting the thickness of the resist and the TiO_2 pillars. 18
3.12 Fabrication steps for an a-Si metasurface. 19
3.13 Isotropic and Anisotropic etching. 22
3.14 Silicon Etching with original recipe. 23
3.15 View of the suspended nickel mask and the nanocylinders fully removed by etching with the original recipe. 23
3.16 Silicon Etching with different recipes. 24
(a) Recipe D 24
(b) Recipe G 24
3.17 Etching of a-Si sample with recipe D. 25

(a) Continuous etching for 5 min. 25
(b) Loop of 5 etching of 1 min. 25
3.18 Ni-mask removal. 25
(a) Sample with Ni-mask before the removal. 25
(b) Sample after the Ni-mask removal. 25

4.1 Schematic view of the experimental setup - DUT: Device Under Test. . . . 27
4.2 View of our setup - DUT: Device Under Test. 27

List of Tables

3.1 Thickness obtained with different spinning tests. 8
3.2 Spinning parameters for TiO_2 sample. 9
3.3 EBL parameters for TiO_2 sample. 9
3.4 DOE for TiO_2 ALD. 12
3.5 Spinning parameters for a-Si sample. 20
3.6 EBL parameters for a-Si sample. 20
3.7 Etching parameters from literature. 22
3.8 Design of Experiment for a-Si etching. 24

Chapter 1

Introduction

In the last decade, metalenses have emerged as a promising technology in optics. Unlike bulky traditional lenses, metalenses offer a flat, lightweight design with exceptional performance. By manipulating light at the nanoscale, they can achieve unprecedented control over light waves, offering advantages such as aberration correction, arbitrary wavefront shaping, and enhanced focusing capabilities.

I completed my internship within the DON group of the MPQ laboratory, which focuses on advanced nanophotonics, optical metasurfaces and nonlinear optics. For the last months, my main task has been to fabricate linear metalenses, experimenting with two materials: amorphous titanium dioxide for the visible range and amorphous silicon for the near-IR. For applications relevant to human vision, titanium dioxide (TiO_2) is a promising candidate because of its high refractive index and transparency at visible wavelengths. Today's state of the art in nanofabrication is provided by a protocol based on atomic layer deposition of amorphous TiO_2 developed at Harvard University [1]. Amorphous silicon is opaque for visible wavelengths, but it is a preferred material for metalenses in the NIR, thanks to its numerous advantage like high refractive index and relatively simple fabrication process. For the fabrication of amorphous silicon metalenses, the most popular technique employed is ICP-RIE (Inductively Coupled Plasma Reactive Ion Etching) [2] [3].

Since the fabrication experience of the DON group is essentially linked to AlGaAs and metallic nanostructures, working with titanium dioxide and amorphous silicon posed new challenges.Therefore, my work has primarily focused on developing protocols to fabricate metalenses using these materials. This report aims to outline the essential steps involved in creating these metasurfaces, drawing on the knowledge and skills acquired during my internship.

The document is organized as follows:

- Chapter 2 provides a concise overview of essential concepts on metasurfaces and metalenses.
- Chapter 3 provides a detailed account of the work I conducted during my internship, including a comprehensive examination of the fabrication steps and technological processes involved in producing metalenses.
- Chapter 4 focuses on the experimental set-up for the characterization of metalenses.

Chapter 2

Theoretical Background

Metamaterials (from the Greek meta, meaning beyond) are artificially engineered materials designed to interact with waves in ways not found in nature. These materials modify the properties of incoming waves as they propagate through their volume. To this end, metamaterials are composed of structures much smaller than the light wavelength, organized in a 3D lattice with sub-wavelength spacing.

2.1 Metasurfaces

Metasurfaces, the 2D counterparts of metamaterials, consist of minuscule structures arranged on a substrate in 2D arrays of subwavelength-spaced optical scatterers, which can be either metallic or dielectric. These scatterers have the capability to modify various characteristics of incident light, exhibiting novel optical properties. By designing these optical scatterers, metasurfaces provide a fundamentally new method of light manipulation. Unlike traditional optics, which rely on refraction, reflection, absorption, and diffraction of light through media with specific refractive indices to control the optical path, metasurfaces achieve light manipulation through the scattering from small nanostructures. The latter interact strongly with light which can be resonantly captured and re-emitted with precise control over phase, polarization and spectrum. To this end, three main strategies can be adopted (fig. 2.1), based on:

- the exploitation of a geometrical phase provided by elements of identical shape and size but different orientation.
- Vertical nanoguides of varying radii, the methodology employed in this study. They can be e.g. conceived as square-shaped dielectric pillars with a square basis width W and height H. These pillars can be organized in a square lattice configuration with a unit cell of size U×U. Each unit cell operates as an element whose effective refractive index $n_{\text{eff}}(W)$ can be modified by adjusting the pillar width W, which controls the confinement of light. Light traveling through each pillar accumulates a phase shift ϕ:

$$\phi = \frac{2\pi}{\lambda} \times n_{\text{eff}} \times H \tag{2.1}$$

  By varying the width W, different values of phase shift can be obtained. To design the metasurface, an array of pillars with gradually varying diameters should be used. This ensures a continuous transition of the phase shift. Covering the full phase range

from 0 to 2π requires designing the pillars so that the variation in their diameters produces a continuous phase shift over this interval [4].

- Huygens nano-disks, with two frequency-degenerated electric and magnetic dipole resonances.

However, geometric phase only works with circularly polarized light while huygens metalenses have very narrow spectral band and present fundamental limitations for beam shaping [5].

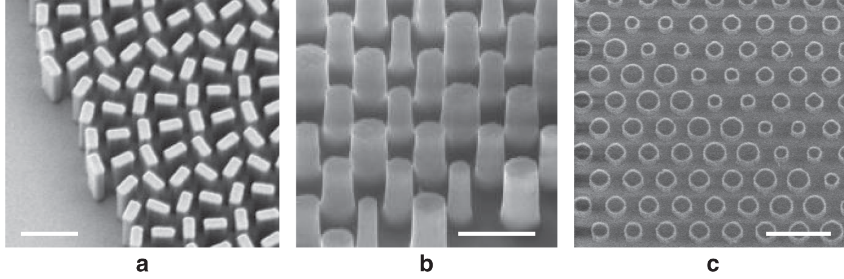

Figure 2.1: (a) Nano-fins used for geometrical phase, (b) Nano-rods used as truncated waveguides and (c) Nano-disks used for Huygens metalens. [6].

2.2 Optical Metalenses

Recently, optical metalenses, a type of metasurface, have gained significant attention for their potential applications in solar energy harvesting, imaging, and optoelectronic devices. Traditional optical devices, such as convex lenses and concave mirrors, have been used for hundreds of years but are often bulky and heavy. These characteristics make them unsuitable for modern electronic and photonic systems that demand miniaturization and integration. In contrast, metasurface lenses offer advantages such as flatness and compatibility with semiconductor manufacturing technology. Metalenses are among the most explored meta-optical elements.

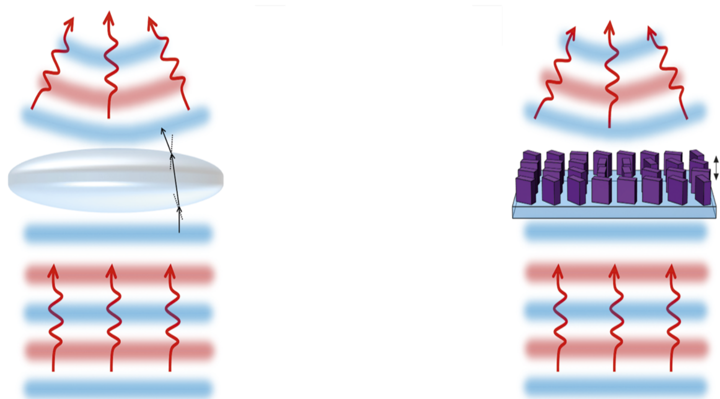

Figure 2.2: Operating mechanisms of refractive lens and metalens [7].

By imparting phase shifts from 0 to 2π, metalenses offer functionalities similar to traditional refractive lenses but with several enhanced capabilities. In particular, they can be thinner

than conventional lenses while maintaining excellent focusing performance. Metalenses may consist of millions of subwavelength unit cells called meta-atoms, which modulate light locally and coherently across the entire metasurface. The shape and size of each meta-atom are determined locally to optimize the overall performance of the metalens. Subwavelength meta-atoms can delay the phase of light, and when properly arranged on the surface, metalenses can produce the same desired phase profile as a classic curved lens.

2.3 State of art

Several materials have been investigated for the fabrication of metalenses. For NIR dielectric metasurfaces, amorphous silicon (a-Si) is explored. D. Visser et al. [3] fabricated metasurfaces based on high refractive index a-Si nanodisk arrays embedded in a flexible and transparent substrate, such as polydimethylsiloxane (PDMS). The fabrication process involved etching the a-Si nanodisk arrays using ICP-RIE (fig. 2.3). Their results show that metasurfaces based on a-Si nanodisk arrays are promising for omnidirectional broadband anti-reflection applications as well as optical filter applications in the NIR wavelength region. Surface reflectivity was measured and simulated for the a-Si nanodisk arrays on a crystalline silicon (c-Si) surface, confirming the broadband anti-reflection capabilities of these metasurfaces, with average surface reflections as low as 7.5%. Additionally, these nanodisk-based metasurfaces could be highly beneficial for both large-scale and micro/nanoscale coloring applications.

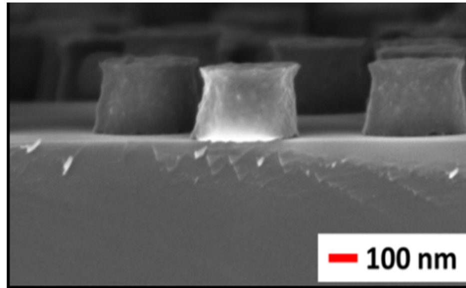

Figure 2.3: Top-view of a substrate-free a-Si nanodisk array on the c-Si surface. [3]

Hu et al. [8] demonstrated mass-producible amorphous silicon metalenses on a 12-inch glass wafer using a complementary metal-oxide-semiconductor compatible process. The measured numerical aperture of the fabricated metalens was 0.496, with a focusing spot size of 1.26 µm at a wavelength of 940 nm. This metalens was integrated into an imaging system to evaluate its resolution, clearly revealing the minimum bar of the resolution chart, which has a width of 2.19 µm. Furthermore, the same system successfully imaged a fingerprint, demonstrating the potential of metalens arrays to shrink the size of future compact consumer electronics.
In the visible spectral region, many types of dielectric materials can be used for designing metalenses, including titanium dioxide (TiO_2). These materials have refractive indices ranging from 2.0 to 2.5. Therefore, the nanostructure design aspect ratio must be sufficiently high to achieve full wavefront manipulation.
For TiO_2, Devlin et al. [1] demonstrated amorphous TiO_2 metasurfaces that maintain

high efficiency across the entire visible spectrum. Their approach to creating metasurfaces uses a bottom-up nanofabrication technique via atomic layer deposition, providing high aspect ratios (fig.2.4).

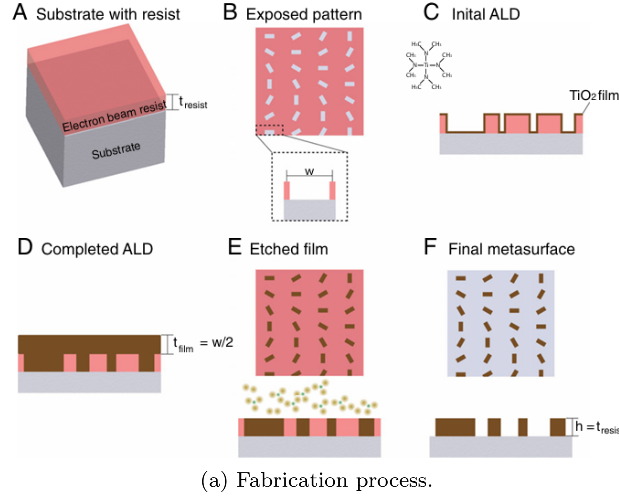

(a) Fabrication process.

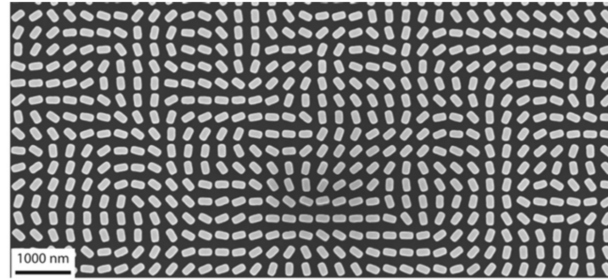

(b) Scanning electron microscope image of fabricated structures - large-scale view of a fabricated metasurface hologram composed of TiO_2 nanofins.

Figure 2.4: Harvard protocol for TiO_2 metalenses [1].

They demonstrated that it is possible to control the phase of a wavefront from 0 to 2π, which is essential for many optical components, and they produced metasurface holograms based on geometric phase.

Liu et al. [9] utilized a titanium dioxide metalens array operating within the visible spectrum to achieve multipole imaging. They introduced a gradient descent algorithm based on cross-correlation to analyze the intensity distribution in the image plane, thereby correcting monochromatic aberrations and enhancing imaging quality. By scrutinizing the aberration-corrected information in the image plane, they accurately determined the 3D coordinates of objects with a relative accuracy ranging from 0.60% to 1.31%. Furthermore, they showcased the metalens array's efficacy in handling arbitrary incident polarization states.

Chapter 3

Nanofabrication

During the internship, the core of my activities was the development of the fabrication process of our metalenses, with the aim of creating them in two different materials: amorphous titanium dioxide and amorphous silicon. In this section the different steps of fabrication of metalenses are presented.

3.1 TiO_2 Metalenses Fabrication

Titanium dioxide (TiO_2) has become a preferred material for applications related to human vision due to its high refractive index and transparency at visible wavelengths (380 nm - 750 nm) [10]. Based on the simulations and design performed at the University of Brescia, a metalens with a diameter of approximately 0.4 mm has been developed. This metalens is composed of TiO_2 nanocylinders on a glass substrate. The nanocylinders have a height of 640 nm, and each square unit cell has a side length of 425 nm, with the nanocylinder positioned at the center of the unit cell. The metalens has a focal length of 500 µm and operates at a wavelength of 600 nm.
The proposed method involves applying a layer of AR-P 6200.13 resist onto a glass substrate using the spin coating technique which results in a thickness of 640 nm. The sample will then be exposed to electron beam lithography (20 kV) to create the desired pattern. After developing the resist, the patterned areas will be filled with titanium dioxide using atomic layer deposition (ALD) [1]. Subsequently, any excess titanium dioxide will be removed through reactive ion etching, and finally, the resist will be stripped away with an O_2 plasma.
The fabrication process is shown in fig. 3.1.

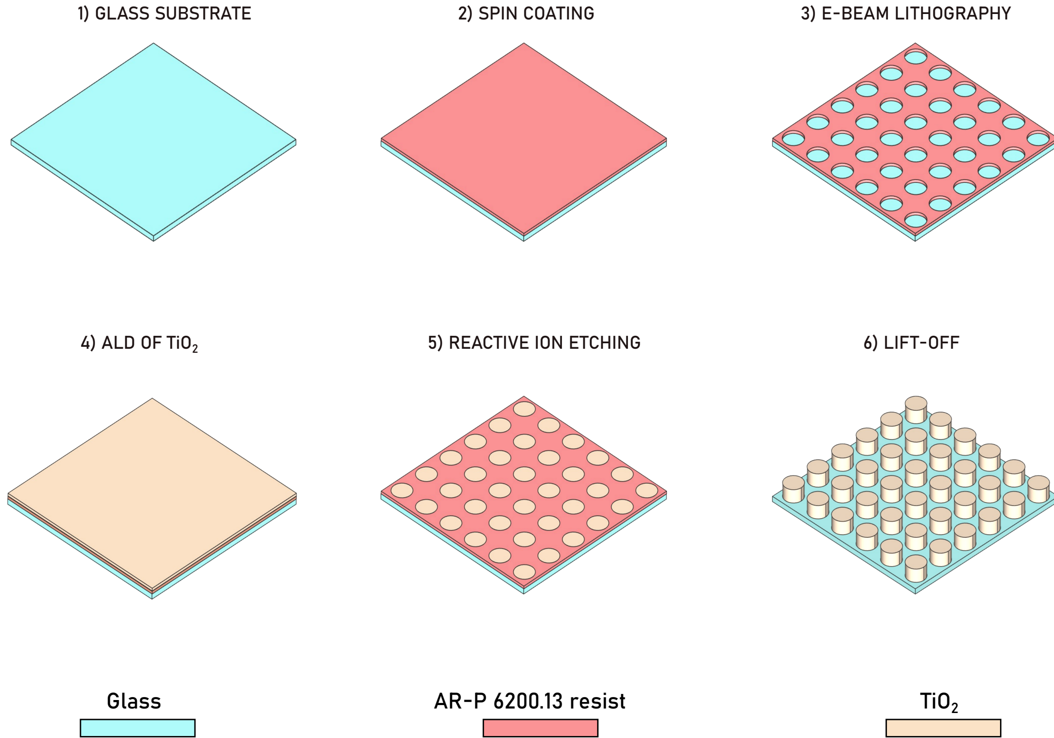

Figure 3.1: Fabrication steps for a TiO_2 metasurface.

3.1.1 Cleaning

The process begins with cleaning the glass substrate. First, the sample is placed in acetone within an ultrasonic bath for five minutes at a temperature between 30 °C and 40 °C. Acetone is a powerful solvent that can dissolve a wide range of organic contaminants. Heating the acetone increases its solvent capacity, making it more effective at dissolving and removing contaminants. In addition, the ultrasonic bath helps to mechanically remove impurities through high-frequency sound waves, allowing for the removal of contaminants that acetone alone cannot achieve. Next, the sample is placed in isopropanol in the ultrasonic bath for two minutes, maintaining the same temperature, to eliminate any remaining impurities and acetone. Finally, a two-minute O_2 plasma treatment is performed to completely remove organic residues and activate the surface for the subsequent resist spin coating.

3.1.2 Spin Coating

The focus then shifts to depositing 640 nm of resist AR-P 6200.13. This thickness is quite uncommon since most spin-coated e-beam resists have thicknesses below 400 nm. Therefore, we carried out several test using the AR-P 6200.13 resist in order to achieve the required thickness. AR-P 6200.13 is a positive electron beam resist, for which the exposed areas of the resist become soluble in the developer.
First, the sample is placed on a hot plate for 4 minutes at 120 °C to remove any aqueous residues. Next, an adhesion promoter, Ti-Prime, is applied to enhance the adhesion of the resist, followed by a baking step at 120 °C for 2 minutes. Then, the resist is spun onto the surface of the sample. Finally, a baking step is performed for 1 minute at 150 °C.

This final baking step is crucial for adequately preparing the resist for the subsequent lithography process, ensuring proper adhesion, stability, and the quality of the desired pattern.
Once the resist has been spin-coated, its thickness is evaluated using reflectometry. This non-destructive analytical technique utilizes reflected light from surfaces and interfaces to measure characteristics such as color intensity, film thickness, and refractive index.

Based on the spin curve shown in fig. 3.2, we considered two options: spinning the resist once at a very low speed or spinning the resist twice at higher speeds to achieve the desired thickness. The thickness measurements are documented in table 3.1, while fig. 3.2 displays the nominal spin curve for the resist. The latter also illustrates the desired thickness we aim to achieve alongside the actual values obtained from various tests. A slightly thicker deposition than the intended thickness isn't problematic, as it's anticipated that during subsequent fabrication steps such as O_2 plasma treatment and reactive ion etching , a portion of either the resist or the TiO_2 layer will likely be removed.

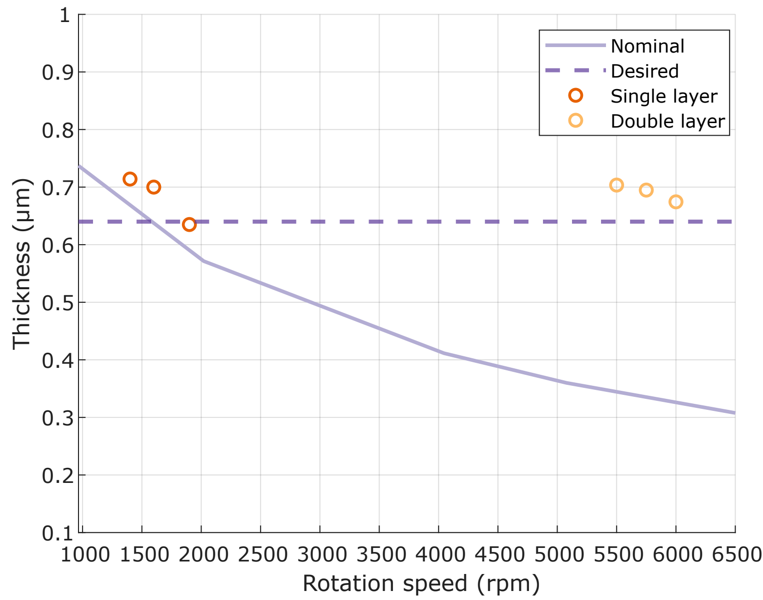

Figure 3.2: Spin curve of AR-P 6200.13.

	Velocity (rpm)	Single layer thickness (nm)	Double layer thickness (nm)
001	1400	714	-
002	1650	700	-
003	1900	635	-
004	5000	-	717.6
005	5500	-	703.5
006	5750	-	694.8
007	6000	-	674.4

Table 3.1: Thickness obtained with different spinning tests.

For the first option, it is observed that spinning at very low speeds results in an irregular

distribution of the resist on the sample surface.
The most effective solution identified involves spinning two layers of AR-P 6200.13 at a speed of 4800 rpm for 60 seconds each. Following the spinning of the resist, a conductive layer, Protective Coating Electra 92 (AR-PC 5090), is applied to the surface to prevent charging effects during lithography. During lithography, the use of the e-beam to expose the resist can induce electrostatic charging on the sensitive surface of the material. These charges can negatively affect the definition and quality of the lithographic pattern, leading to distortions or defects in the final shape. The Electra 92, typically composed of materials such as a thin layer of metal, serves as an electrical ground, dissipating the electrostatic charges and maintaining the resist surface neutral and stable during exposure. This helps ensure better definition and precision in the details of the final lithographic pattern. The spinning parameters for all the components, including the adhesion promoter, resist, and conductive layer, are summarized in table 3.2.
The final step involves baking for 2 minutes at 90 °C.

Spinning parameters	Step 1	Step 2
Ti-prime	500 rpm - 3 sec	4000 rpm - 30 sec
AR-P 6200.13	500 rpm - 3 sec	4800 rpm - 60 sec
Electra 92	500 rpm - 3 sec	4000 rpm - 60 sec

Table 3.2: Spinning parameters for TiO_2 sample.

3.1.3 Electron Beam Lithography

Electron Beam Lithography (EBL) is a precise direct writing technique that utilizes a focused beam of electrons to expose a radiation-sensitive resist, eliminating the need for a mask. Unlike traditional photolithography, EBL encounters minimal diffraction and offers high levels of automated and precise control. In EBL, the electron beam selectively alters the solubility of the resist, enabling the subsequent removal of either the exposed (positive resist) or non-exposed regions (negative resist) through immersion in a solvent (development). The wafer coated with resist is introduced into an electron microscope during EBL, where the electron beam functions like a pen, delineating and disrupting the chemical bonds of the polymer. The objective is to create minute structures in the resist, which can then be transferred to the substrate material. The primary advantage of EBL is its capability to produce custom patterns with sub-10 nm resolution, making it ideal for applications requiring intricate features. However, its throughput is relatively low. During the lithography process, several factors demand great care, including sample alignment (origin correction and angle correction), scanning electron microscope (SEM) column parameters (focus, astigmatism, optical axis centering), parameters and alignment on the writing field, and e-beam resist dose. The most important parameters are summarized in table 3.3

Aperture	10 µm
Voltage	20 kV
WritingField	100 µm
Dose	200 µC/cm^2

Table 3.3: EBL parameters for TiO_2 sample.

The initial pattern implemented consists of a series of nanocylinders with varying diameters, each subjected to different dose factors. This approach is employed to determine the optimal dose required for achieving the desired exposure. Notably, with significantly thicker resist layers, the correct dose needed to expose all the resist is considerably higher than the nominal dose ($50\,\mu C/cm^2$). In other words, with a low dose, not all of the resist depth is exposed, leading to some unexposed volumes that retain their original solubility and persist on the substrate even after development (fig. 3.3).

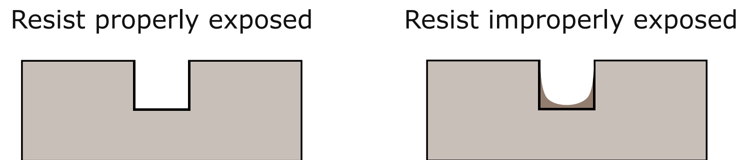

Figure 3.3: Example of well-developed and fully exposed resist versus incompletely developed resist due to insufficient exposure.

3.1.4 Development

After the lithography, the sample undergoes a series of steps for resist development. Initially, it is immersed in water for 1 minute to remove the Electra 92. Subsequently, it undergoes a 1 minute and 30 second immersion in the developer MIBK-IPA, followed by another 1 minute and 30 second immersion in isopropanol to stop the action of the developer. However, it is observed that not all the resist is fully developed. This issue likely arises from performing a double spin, whereby the first layer undergoes two baking steps and is overbaked, making it difficult to develop completely. Another possibility is that the exposure dose may not be sufficient to fully expose the entire resist thickness. Consequently, not all of the exposed resist undergoes a change in solubility and remains intact during the development process.

3.1.5 Atomic Layer Deposition

Let us now focus on the deposition of titanium dioxide through the atomic layer deposition (ALD) technique. ALD is a thin-film deposition method that relies on a sequential gas-phase chemical process and falls under a subclass of chemical vapor deposition. In ALD, two chemicals known as precursors, or reactants, are utilized. These precursors interact with the material surface individually, in a sequential and self-limiting manner. This process results in the gradual deposition of a thin film through repeated exposure to alternating precursors. Unlike chemical vapor deposition, the precursors are never present simultaneously in the reactor; instead, they are introduced in separate, non-overlapping pulses. Each pulse enables the precursor molecules to react with the surface in a self-limiting manner, terminating once all available surface sites are consumed. As a result, the amount of material deposited on the surface after a single exposure to all precursors (termed an ALD cycle) is determined by the nature of the precursor-surface interaction. By adjusting the number of cycles, it is possible to achieve uniform and precise growth of materials on arbitrarily complex and large substrates. Moreover, ALD provides conformal coverage and monolayer control over film thickness. Its conformal nature is critical for producing high aspect-ratio nanostructures. Finally, films produced via ALD exhibit smoother surfaces with fewer defects compared to those prepared using sputtering or

evaporation techniques. An example of a tipical ALD process in shown in fig. 3.4. In our case ALD enables precise control over the material phase of the deposited titanium dioxide, which results in amorphous, rutile, or anatase films, depending on the deposition temperature. Our precursor of choice is tetrakis(dimethylamido)titanium (TDMAT) due to its high deposition rate and absence of defect-driven absorption commonly associated with $TiCl_4$-based precursors [11].

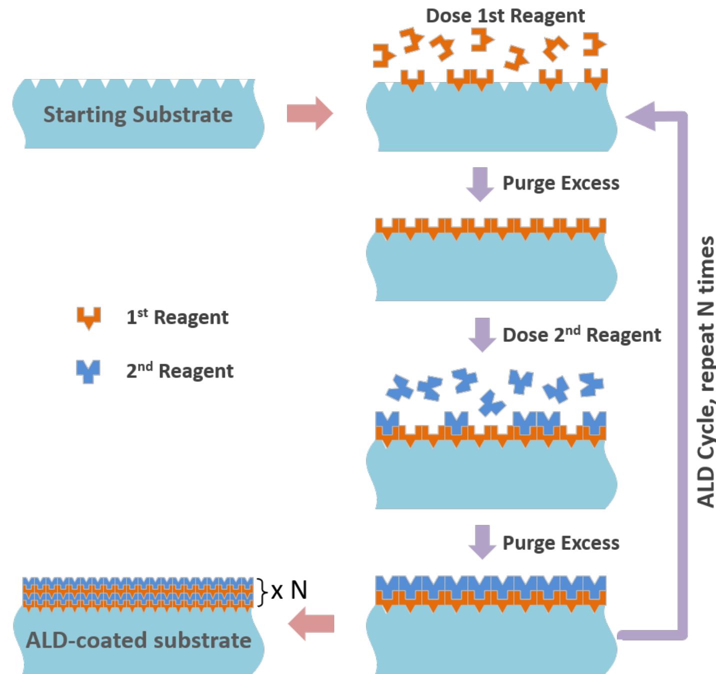

Figure 3.4: Atomic Layer Deposition Process [12].

Our aim is to deposit amorphous titanium dioxide, following the process developed by the Capasso's group at Harvard [1]. We adopted and optimized this recipe to our specific clean-room through the statistical technique of design of experiments (DOE), which enables manipulation of multiple input factors to determine their effect on a desired output (response). By adjusting several inputs simultaneously, DOE can reveal important interactions that might be overlooked when experimenting with one factor at a time.
To refine the process, 10 samples with a silicon substrate, which is more more readily available than glass and simplifies the subsequent ellipsometry measurement, are fabricated, varying key parameters from the reference recipe. These parameters include:

- Number of TDMAT pulses
- Number of H_2O pulses
- Ultra fast (UF) valve aperture time
- TDMAT purge time
- H_2O purge time
- Temperature

For this initial analysis, a total of 250 cycles were executed to achieve a titanium dioxide layer deposition of approximately 20 nm thickness. The chamber pressure was maintained at 250 mTorr. Before the deposition of TiO_2, the sample undergoes a 15-second treatment with O_2 plasma. The latter chemically activates the substrate surface, enhancing its surface energy and facilitating the adhesion and reaction of ALD precursors on the surface. Oxygen plasma can also effectively eliminate organic contaminants or other impurities present on the substrate surface, ensuring a cleaner and more reactive surface for the subsequent ALD process. In table 3.4 are summarized all the recipes analyzed.

n.	TDMAT pulses	H_2O pulses	UF valve (ms)	TDMAT purge (ms)	H_20 purge (ms)	Temp. (°C)
001	2	1	400	10000	7000	70
002	2	1	400	10000	7000	90
003	2	1	1000	7000	10000	70
004	1	2	1000	7000	7000	70
005	1	2	400	10000	10000	70
006	1	1	400	7000	10000	90
007	2	2	400	7000	7000	90
008	1	1	1000	10000	7000	90
009	2	2	1000	10000	10000	90
010	1	2	2000	15000	15000	90

Table 3.4: DOE for TiO_2 ALD.

After fabricating the samples, X-ray diffraction (XRD) analysis is conducted to confirm the amorphous nature of TiO_2. XRD is a technique employed in materials science to discern the atomic and molecular structure of a substance. It involves irradiating a sample of the material with X-rays and subsequently measuring the intensities and angles of the X-rays scattered from the material. The resulting intensity of the scattered X-rays is graphed against the scattering angle, and the material structure is ascertained by analyzing the positions, angles, and intensities of the scattered intensity peaks. During XRD analysis, X-rays are scattered by the atomic planes of the sample, and the resultant diffraction peaks provide details regarding the interplanar distance between atoms in the material and their periodic arrangement. In case of amorphous TiO_2, the absence of an ordered crystalline structure leads to a broad diffraction pattern of X-rays devoid of distinct peaks. Consequently, through XRD analysis, it becomes feasible to discern whether TiO_2 is amorphous by observing the dearth of characteristic diffraction peaks associated with crystalline phases, thereby indicating the presence of a disordered and non-crystalline structure. The measurement results show only peaks due to the silicon substrate, with no peaks attributable to titanium dioxide, indicating that the TiO_2 is amorphous.(fig. 3.5).

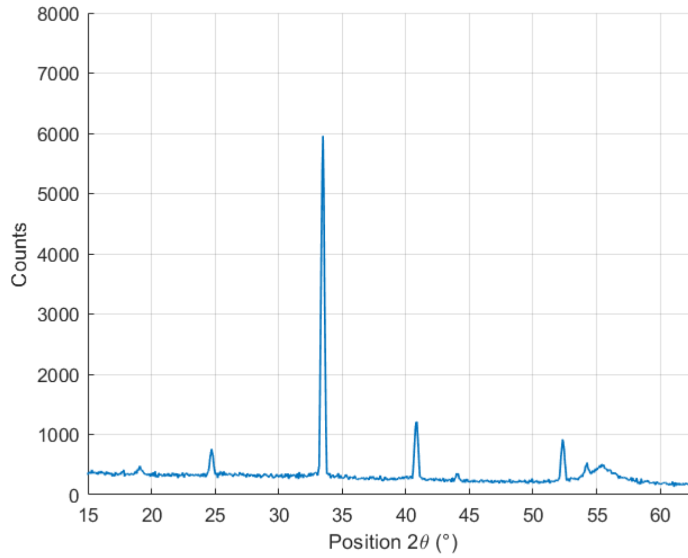

Figure 3.5: XRD analysis on sample 002 - peaks originate from the silicon substrate.

Afterward, ellipsometry is conducted to measure the deposited thickness and refractive index. This technique is used to explore the dielectric properties of thin films, such as their complex refractive index or dielectric function. It relies on detecting changes in the polarization state of a light beam after it is reflected by or transmits through the material. By analyzing these changes, both the film thickness and optical properties can be determined. Ellipsometry focuses on ellipsometric angles Ψ and Δ, which relate to the ratio of complex Fresnel reflection coefficients r_s (for light polarized perpendicular to the plane of incidence) and r_p (for light polarized parallel to the plane of incidence). This is expressed by the fundamental equation of ellipsometry:

$$\rho = \frac{r_p}{r_s} = \tan(\Psi) \exp i\Delta \tag{3.1}$$

where

$$\tan(\Psi) = \frac{|r_p|}{|r_s|} \qquad 0^\circ \leq \Psi \leq 90^\circ \tag{3.2}$$

and

$$\Delta = \delta_p - \delta_s \qquad 0^\circ \leq \Delta \leq 360^\circ \tag{3.3}$$

Thus, Δ is the phase shift between parallel and perpendicular polarized light and Ψ is the amplitude component.

The results obtained , shown in fig. 3.6, are consistent with literature [1]. At a wavelength of 600 nm, the k value is nearly zero, while the n value is around 2.2 across all recipes. These values of n and k made possible the realization of metalenses in visible range

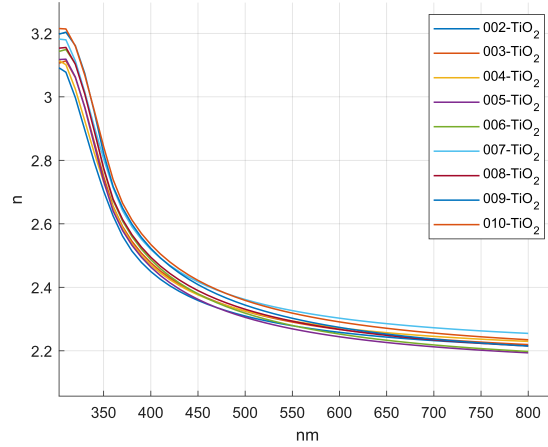

(a) Real part of refractive index.

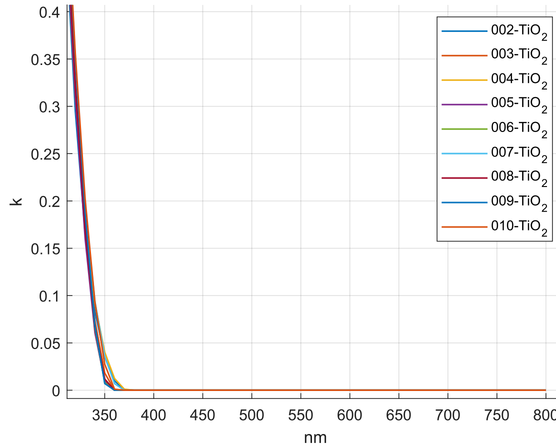

(b) Imaginary part of refractive index.

Figure 3.6: Real and imaginary part of the refractive index n+ik, as measured on the TiO_2 films fabricated according to our recipes.

Let us use box plots to graphically represent the thicknesses obtained as a function of each parameter analyzed in the design of experiment investigation. These plots illustrate the distribution of thicknesses for two values of each parameter, highlighting the median. By comparing the medians between all these pairs of values, it appears that temperature and H_2O purge time are the parameters that most significantly influence the final film thickness (fig. 3.7).

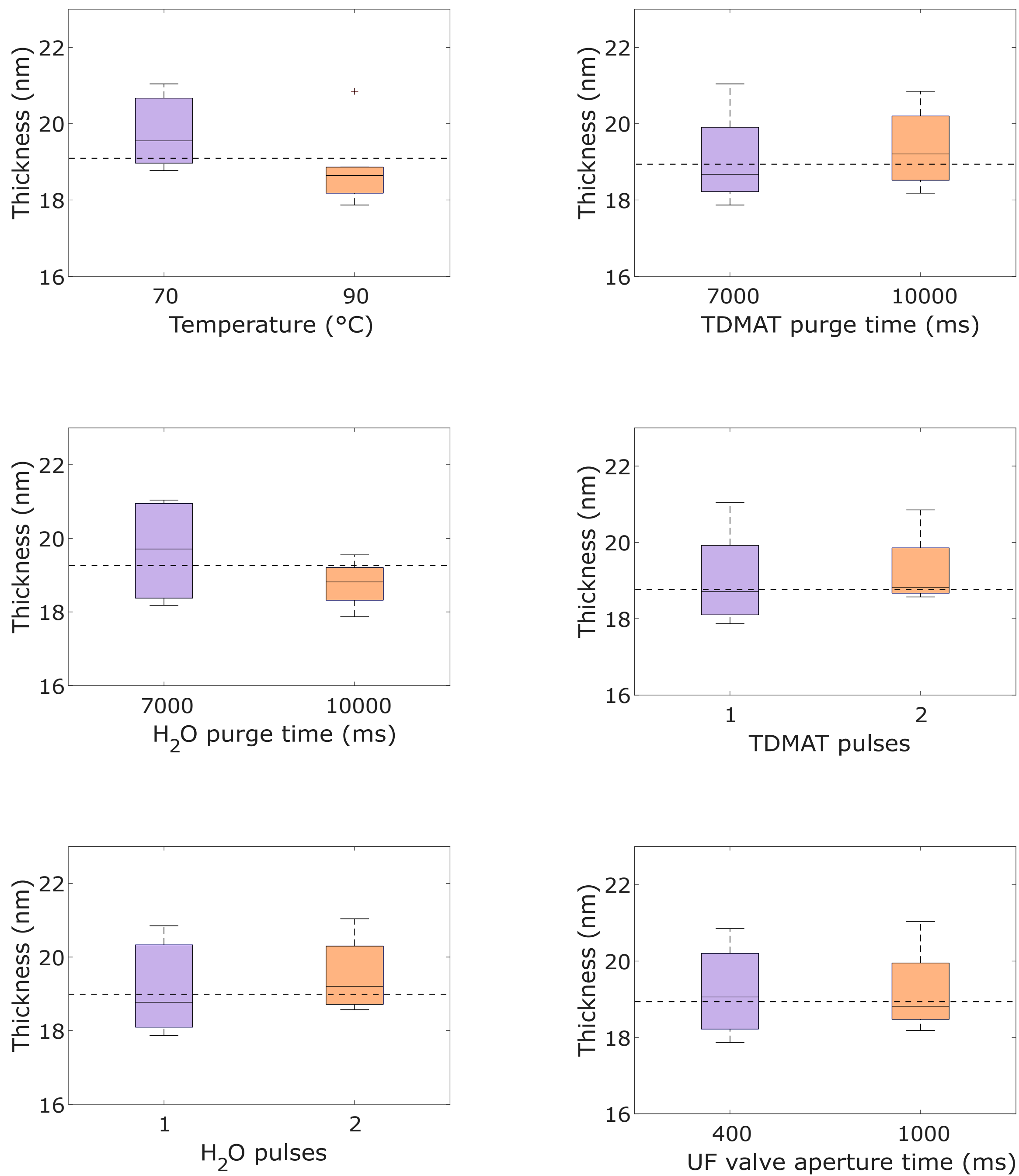

Figure 3.7: DOE BoxPlot for TiO_2 tests. Temperature and H_2O purge time are the parameters that most significantly influence the final thickness.

Based on these results, our optimization resulted in the following protocol:

- TDMAT : 2 pulses
- H2O : 1 pulses
- TDMAT purge time : 10000 ms
- H2O purge time : 10000 ms

- UF valve aperture time : 400 ms
- Temperature : 90 °C

2251 cycles are executed to achieve a TiO_2 thickness of 136 nm, yielding a refractive index of 2.48 at a wavelength of 600 nm, as determined by ellipsometer analysis (see fig. 3.8).

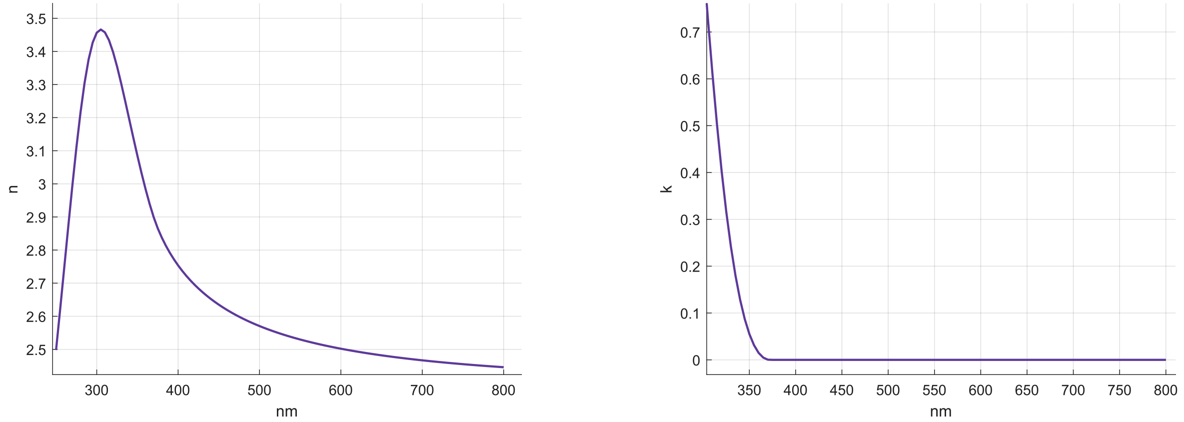

Figure 3.8: Measured real and imaginary part of the complex refractive index as a function of wavelength.

3.1.6 Reactive Ion Etching

To eliminate the excess of TiO_2, I refined a new protocol based on the methodology outlined in [13], incorporating the following parameters:

- SF_6: 10 sscm
- CHF_3: 50 sccm
- Pressure: 50 mTorr
- RF Power: 50 W

Laser interferometry serves as an *in-situ* method for determining etch rates and identifying heterolayers during reactive ion etching (RIE). It monitors changes in interference patterns of reflected light waves as the material undergoes variations in composition and thickness. For normal incidence of the laser beam, the thickness of the material removed between two consecutive periods of laser interferometry signal is given by $\Delta d = \lambda/(2n)$, where λ represents the wavelength of the laser beam and n denotes the refractive index of the material. Changes in signal values indicate transitions between materials, while alterations in signal periods reflect variations in etch rates during layer etching.
Monitoring the interferometer signal enables the identification of the point when TiO_2 is fully removed, signaling the transition to the etching of the AR-P 6200.13 resist (fig. 3.9). Utilizing this information, the process is stopped at the interface between TiO_2 and AR-P 6200.13.

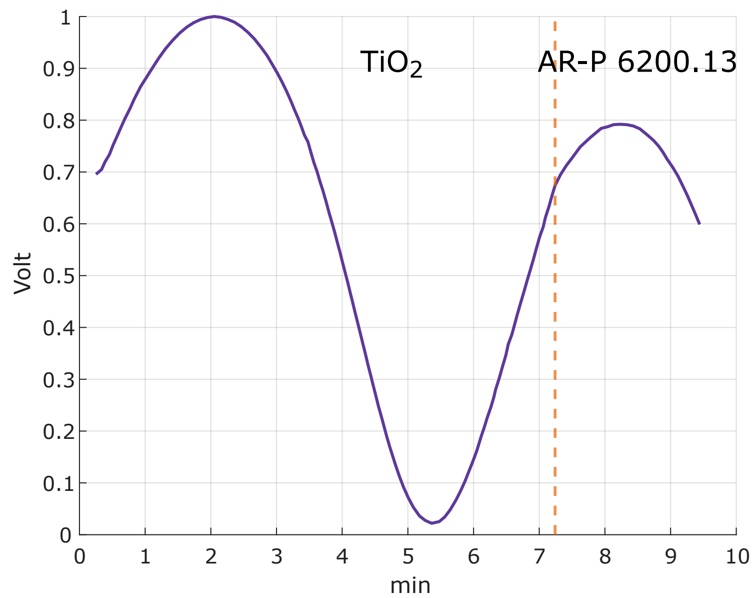

Figure 3.9: Interferometric signal highlighting the transition between TiO_2 and AR-P 6200.13.

For the last step, to remove the AR-P 6200.13 and preserve only the TiO_2 nanopillars, an O_2 plasma treatment is conducted using RIE.
The resulting sample is displayed in fig. 3.10.

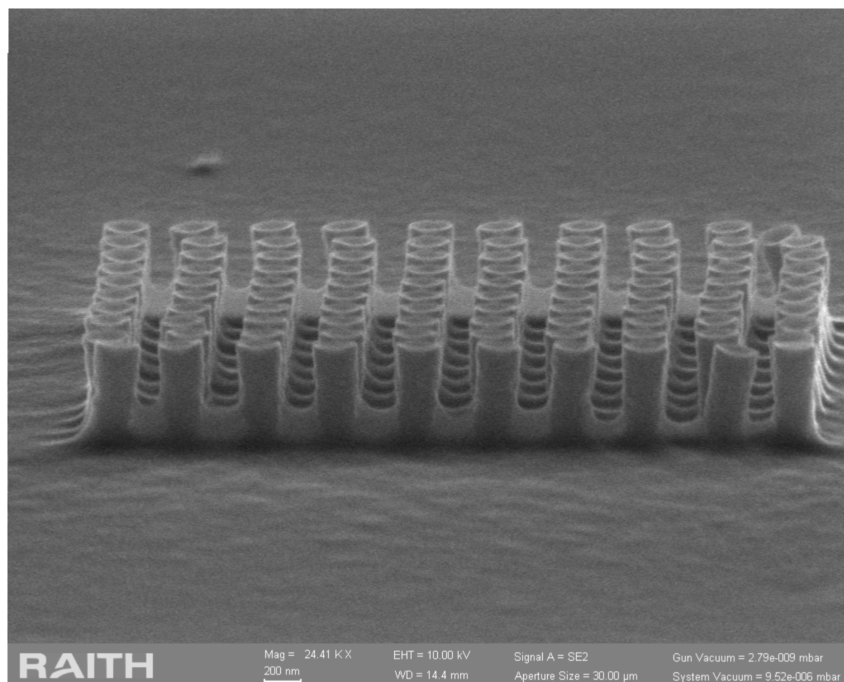

Figure 3.10: SEM observation of the final sample.

As evident from the image, there is still some work to do to optimize the fabrication process. Probably not all the resist was removed during the development phase, resulting in a final pillar height significantly lower than desired (fig. 3.11).

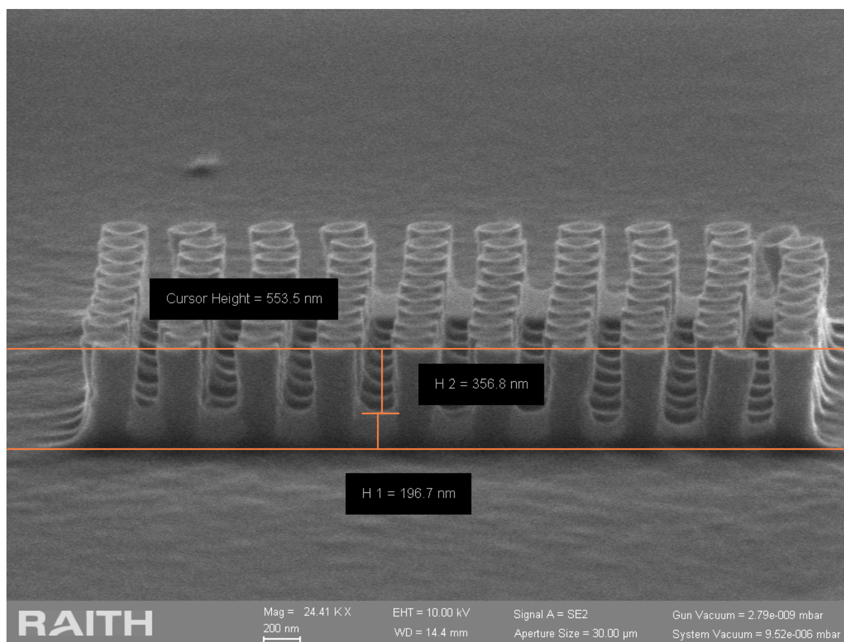

Figure 3.11: SEM imaging of the final sample, highlighting the thickness of the resist and the TiO_2 pillars.

3.2 a-Si Metalenses Fabrication

Amorphous silicon is preferred for creating metalenses in the NIR. With its high refractive index, it plays a crucial role in precisely manipulating light phase at the nanoscale. Importantly, silicon can achieve competitive efficiency levels and boasts a relatively simple fabrication process. As in the case of titanium dioxide, through simulations and design by the University of Brescia, a metalens with a diameter of approximately 0.4 mm has been developed. The nanocylinders have a height of 850 nm. The unit cell is square with a side length of 350 nm, and each nanocylinder is positioned at the center of its unit cell. This metalens operates at a wavelength of 900 nm. For the amorphous silicon process, the procedure begins with an amorphous silicon substrate, on which PMMA (200 nm) is deposited as a resist. Next, electron beam lithography at 20 kV is used to create the desired pattern. After development, a 40 nm layer of Ni is deposited, followed by a lift-off process in acetone for several hours to remove all the resist. Finally, RIE is performed trying to produce perfectly vertical pillars.
The fabrication process is shown in fig. 3.12.

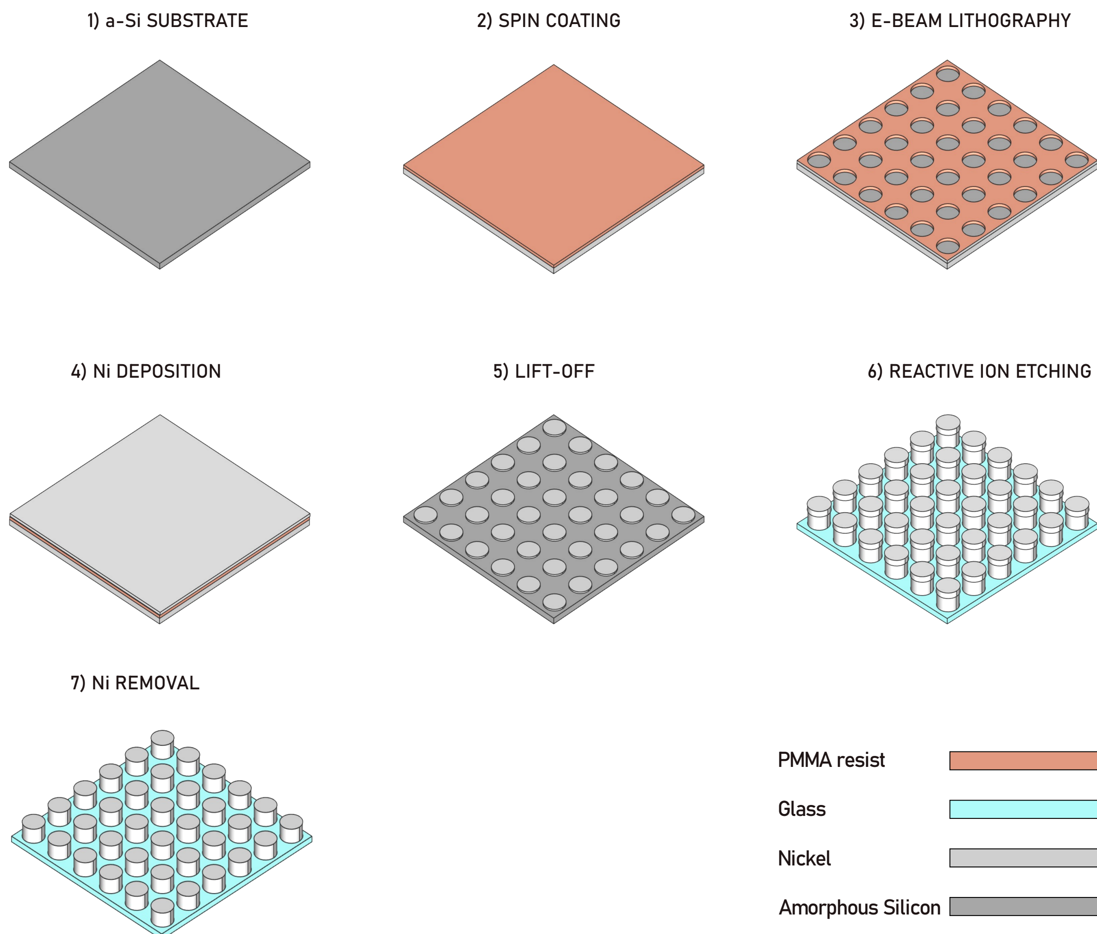

Figure 3.12: Fabrication steps for an a-Si metasurface.

3.2.1 Cleaning

The process begins with cleaning the amorphous silicon substrate. The same procedure as that for the TiO_2 sample is followed.

3.2.2 Spin Coating

Then, the sample is placed on a hot plate at 120 °C for 4 minutes to remove any aqueous residues. Next, the PMMA resist is spun onto the surface of the sample. PMMA is a positive electron beam resist, meaning the exposed areas become soluble in the developer. Following this, the resist underwent a baking step at 180 °C for 1 minute. After spinning the resist, Protective Coating Electra 92 (AR-PC 5090) is applied to the surface to prevent charging effects during lithography as for the TiO_2 sample. The final step involves baking for 2 minutes at 90 °C. The spinning parameters for all the steps are summarized in table 3.5.

Spinning parameters	Step 1	Step 2
PMMA	500 rpm - 3 sec	5000 rpm - 30 sec
Electra 92	500 rpm - 3 sec	4000 rpm - 60 sec

Table 3.5: Spinning parameters for a-Si sample.

3.2.3 Electron Beam Lithography

Subsequently, the desired pattern is transferred onto the sample using electron beam lithography. The initial pattern implemented features a series of nanocylinders with varying diameters, each undergoing different dose factors. This approach serves to pinpoint the optimal dose necessary for achieving precise exposure. Additionally, rectangular shapes with a width of 4 µm are incorporated into the pattern to simplify the assessment of subsequent etching quality. The values of the most important parameters are summarized in table 3.6.

Aperture	10 µm
Acceleration Tension	20 kV
WritingField	100 µm
Dose	220 µC/cm^2

Table 3.6: EBL parameters for a-Si sample.

3.2.4 Development

Immediately after lithography, the sample is immersed in water for one minute to remove the Electra 92. It is then placed in MIBK-IPA for 30 seconds, followed by another 30 seconds in Isopropanol.

3.2.5 Metal deposition

After the development of the resist, a layer of nickel, approximately 40 nm thick, is deposited on the sample surface using an evaporator. Evaporation, a widely employed

method of thin-film deposition, involves vaporizing the source material within a vacuum environment. The resulting vapor particles then travel directly to the target object (substrate), where they condense back into a solid state. This technique finds applications in both microfabrication and the production of macro-scale products, such as metallized plastic film. The deposited nickel layer serves as a protective mask during the etching process. Specifically, during silicon etching, the regions covered by nickel remain unaffected.

3.2.6 Lift-Off

In microstructuring technology, the lift-off process is employed to create patterns of a target material on the surface of a substrate, utilizing a sacrificial material such as resist. Unlike traditional subtractive techniques like etching, this process is additive in nature. During the lift-off process, a sacrificial material, commonly referred to as "resist", is initially deposited onto the substrate surface. Subsequently, the target material is deposited on top of the resist. Once the deposition of the target material is complete, the resist is removed, effectively lifting it off from the surface along with the overlaid material. This leaves behind only the desired target material on the substrate's surface, thus creating the intended pattern. The lift-off process is frequently employed in applications requiring a high degree of precision and control in the formation of microscopic or nanoscopic structures.
To perform the lift-off, the sample is immersed in acetone for approximately three hours, facilitating the removal of the resist.

3.2.7 Reactive Ion Etching

The most challenging step is certainly the etching of amorphous silicon. Our approach involves starting with Capacitively Coupled Plasma Reactive Ion Etching (CCP-RIE), as this equipment is available in our lab's cleanroom. Reactive-ion etching (RIE) is a dry etching technique used in microfabrication, which utilizes chemically reactive plasma to remove material from wafers. The plasma is generated under low pressure (vacuum) by an electromagnetic field. High-energy ions from the plasma bombard the wafer surface and react with it. Plasma is initiated in the system by applying a strong RF (radio frequency) electromagnetic field to the wafer platter. The oscillating electric field ionizes the gas molecules by stripping electrons from them, creating a plasma. During each cycle of the field, electrons are accelerated up and down within the chamber, occasionally striking both the upper wall of the chamber and the wafer platter. Meanwhile, the much more massive ions move relatively little in response to the RF electric field. When electrons are absorbed into the chamber walls, they are simply grounded and do not affect the electronic state of the system. However, electrons deposited on the wafer platter cause it to build up charge due to its DC isolation. This charge accumulation develops a large negative voltage on the platter, typically around a few hundred volts. The plasma itself develops a slightly positive charge due to the higher concentration of positive ions compared to free electrons. Due to the significant voltage difference, positive ions drift toward the wafer platter, where they collide with the samples to be etched. The ions react chemically with the surface materials of the samples and can also dislodge (sputter) material by transferring some of their kinetic energy. Compared to ICP-RIE technology used in [3], which achieves perfectly vertical sidewalls and ensures anisotropic etching, the latter is more challenging with CCP-RIE. In fact, using CCP-RIE can result in isotropic etching, which means that the material is etched uniformly in all directions. This can lead to underetching, where

the material is removed not only vertically but also horizontally beneath the mask. As a result, the etching process can extend laterally, creating an over-etched region under the mask, and compromising the precision of the pattern transfer. An example of isotropic and anisotropic etching is shown in fig. 3.13.

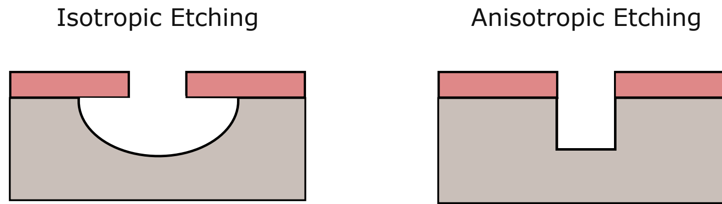

Figure 3.13: Isotropic and Anisotropic etching.

Etch conditions in a RIE system are highly dependent on various process parameters, such as pressure, gas flows, and RF power.
Fluorinated gases, typically CHF_3 and SF_6, are used to etch silicon. The anisotropic etch mechanism relies on an ion-enhanced inhibitor etching process, which requires three components:

1. reactive neutral species,
2. inhibitor film-forming species,
3. vertical ion flux to the substrate to prevent growth or etch the inhibitor film on horizontal surfaces.

These mechanisms can be controlled more or less independently by the three etch gases:

- F_6 produces F radicals for the chemical etching of silicon.
- 0_2 creates O radicals that passivate the silicon surface with silicon oxide species.
- CHF_3 produces CF_x ions which, along with SF_x ions, suppress the formation of the passivation layer on horizontal surfaces.

Literature provides some recipes that have successfully achieved vertical sidewalls (table 3.7).

	SF_6 (sccm)	O_2 (sccm)	CHF_3 (sccm)	Pressure (mTorr)	RF power (W)
Recipe from [14]	30	20	-	43	240
Recipe from [15]	25	25	10	7	150
Recipe from [16]	30	10	12	100	100
Previous recipe from cleanroom's machine	25	10	10	100	100

Table 3.7: Etching parameters from literature.

First, I began by attempting to perform the etching using the pre-existing recipe in the machine. For this preliminary test, I used silicon substrates, which are more readily available compared to amorphous ones. The sample is etched for approximately 10 minutes to achieve the desired thickness. As shown in fig. 3.14, there is significant underetching, and the sidewalls are not vertical.

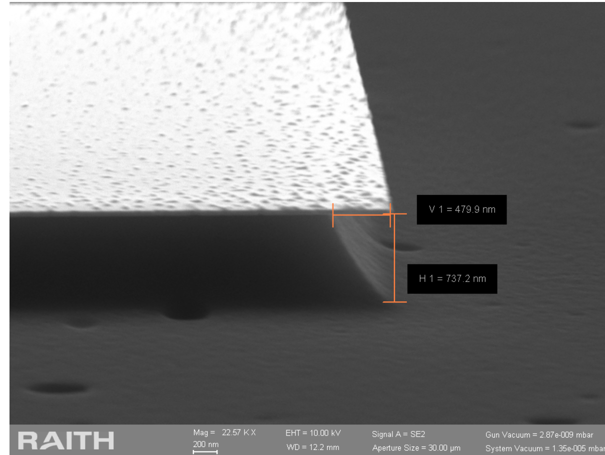

Figure 3.14: Silicon Etching with original recipe.

The issue arises because the underetching is so severe that it exceeds the diameter of our nanocylinders. Consequently, the silicon of our nanocylinders is completely removed beneath the Nickel mask. As seen in fig. 3.15, the nickel masks become detached, leaving no silicon cylinders beneath them.
Same result was obtained on the a-Si sample.

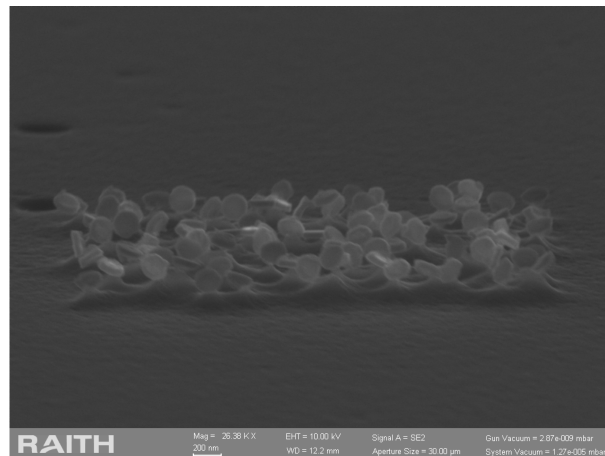

Figure 3.15: View of the suspended nickel mask and the nanocylinders fully removed by etching with the original recipe.

Upon reviewing the literature, it turned out that the parameters required to achieve anisotropic and vertical etching vary across different recipes. For example, in some cases, the pressure is very low, while in others it is very high. To address this, we employed again the DOE technique. Starting with the existing recipes, we varied key parameters such as gas concentrations (SF_6, O_2, CHF_3), pressure, and RF power. Initially, a total of 16 silicon samples were fabricated to explore different combinations of these parameters (table 3.8).

n.	SF_6 (sccm)	O_2 (sccm)	CHF_3 (sccm)	Pressure (mTorr)	RF power (W)
A	25	10	50	100	240
B	25	0	50	100	60
C	25	0	5	100	240
D	10	10	5	20	60
E	10	10	5	100	240
F	10	10	50	20	240
G	10	0	50	20	60
H	25	10	50	20	60
I	10	0	5	100	60
L	25	10	5	20	240
M	10	10	50	100	60
N	25	0	5	20	60
O	10	0	5	20	240
P	25	0	50	20	240
Q	10	0	50	100	240
R	25	10	5	100	60

Table 3.8: Design of Experiment for a-Si etching.

Some of these recipes (F, I, O, Q, P) prove to be unstable, so only the remaining stable ones are tested. Before each etching test, an O_2 plasma treatment is performed on every sample for 1 minute to ensure that all resist is removed during the lift-off step. Each recipe is then tested for 1 minute. The most promising recipes are D and G, as shown in fig. 3.16. This result is probably due to the lower pressure in the chamber. Lower pressure increases the mean free path of the ions, contributing to a more vertical etching direction. In fact, at lower pressures, the ions accelerated by the electric field move more perpendicularly to the substrate surface. This reduces the probability of collisions with gas molecules before reaching the surface, leading to a more anisotropic and less lateral attack. Consequently, this favors the formation of more vertical sidewalls.

(a) Recipe D (b) Recipe G

Figure 3.16: Silicon Etching with different recipes.

After just one minute of etching, the sidewalls appear to be vertical. Subsequently, recipe D is tested on amorphous silicon: one sample undergoes continuous etching, following the interferometer signal to etch through all the material, while the second sample is subjected to five cycles of etching, each lasting one minute. However, with increasing etching time, the etching process unfortunately reverts to being isotropic, resulting in significant underetching (fig. 3.17). The same phenomenon is observed with recipe G.

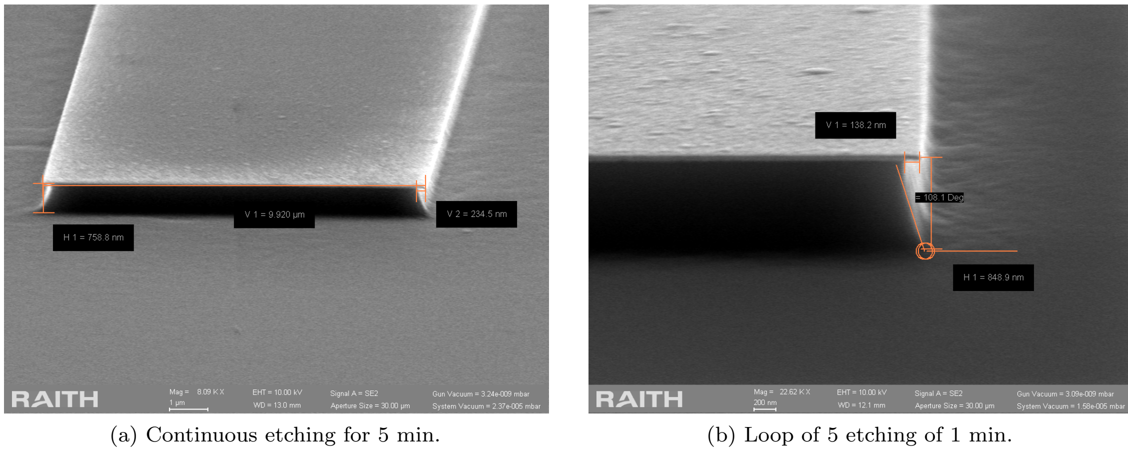

(a) Continuous etching for 5 min.

(b) Loop of 5 etching of 1 min.

Figure 3.17: Etching of a-Si sample with recipe D.

Compared to the initial recipe, the current outcome shows improvement. Specifically, in the etching with the loop, we observe reduced horizontal etching. Nevertheless, further refinement is necessary to develop a comprehensive and effective protocol.

3.2.8 Nickel removal

The nickel mask is effectively removed using an acidic aqueous solution including $FeCl_3$ (30% $FeCl_3$ + 3% HCl) [17]. As depicted in fig. 3.18, the nickel mask (the film covering the silicon columns) is entirely dissolved, and the silicon surface appears unperturbed.

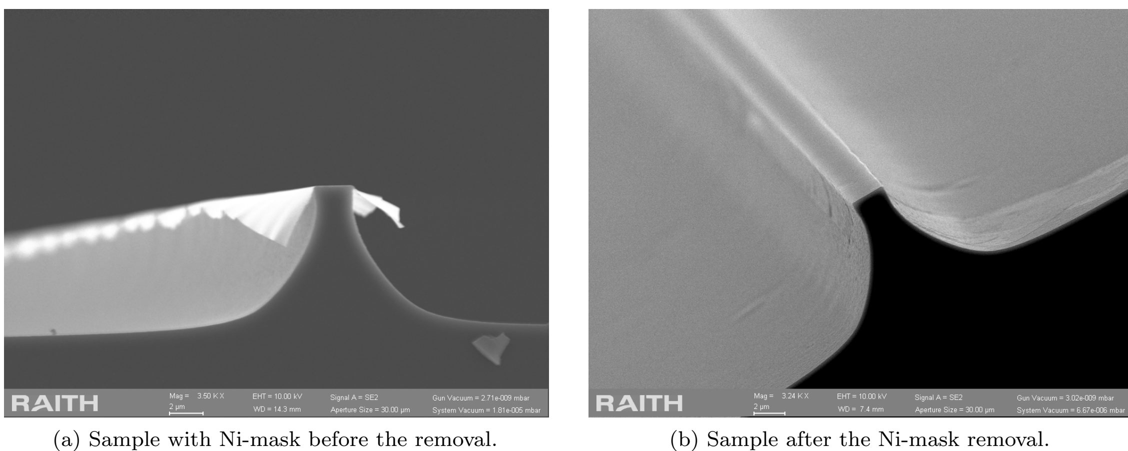

(a) Sample with Ni-mask before the removal.

(b) Sample after the Ni-mask removal.

Figure 3.18: Ni-mask removal.

Chapter 4

Experimental Set-up

The fabricated metalenses need to be characterized in order to evaluate their optical performances. A commonly used metric is the Encircled Energy (EE) which quantifies the energy density at the focal spot. EE is intricately linked to the Point Spread Function (PSF), which describes how a point source of light is distributed in the image plane due to aberrations and diffraction. Consider observing an infinitely small emitting object, such as a star, through a lens undergoing testing. The lens will necessarily aberrate the spot and create a point spread function (PSF). In ideal conditions, a "perfect" lens forms an Airy disc. EE quantifies the fraction of the total energy of the light beam contained within a specified radius from the PSF [18].
I have started mounting an optical bench for this type of measurement that is not complete yet.
To measure the EE, a generic measurement setup (fig. 4.1) is implemented with the following key elements:

1. Laser source with appropriate wavelength for metalenses (TiO_2 - visible range, a-Si - near-infrared)

2. Calibrated pinholes: This is a pinhole wheel made of optical glass. The pinholes are etched on an opaque chromium coating deposited on a fused silica flat substrate. The transmission of the substrate must be taken into account when evaluating the overall transmission through the pinhole aperture. The available pinholes have diameters ranging from 25 to 2000 µm

3. Sample to be examined (DUT: Device Under Test)

4. Power meter: the sensing unit is a silicon photodiode coupled with a digital measurement console. The sensor operates between 400 nm and 1100 nm.

In our particular case (fig. 4.2), we began by using a helium-neon laser operating at a wavelength of 543 nm. To achieve precise beam alignment, we employed two irises and two mirrors. Following this, we positioned the lens on a motorized stage to determine the optimal focal distance respect to the calibrated pinholes and the power meter. Throughout the setup, a camera was employed to verify the accurate alignment of the beam within the pinholes and the lens.

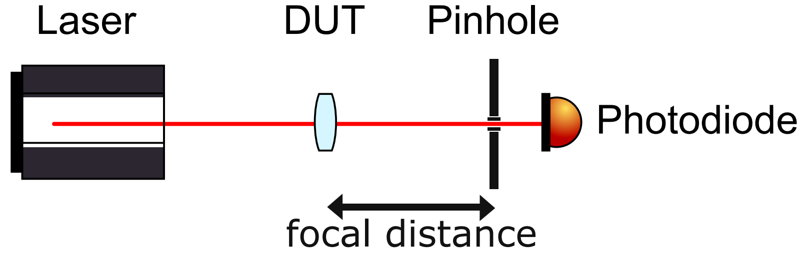

Figure 4.1: Schematic view of the experimental setup - DUT: Device Under Test.

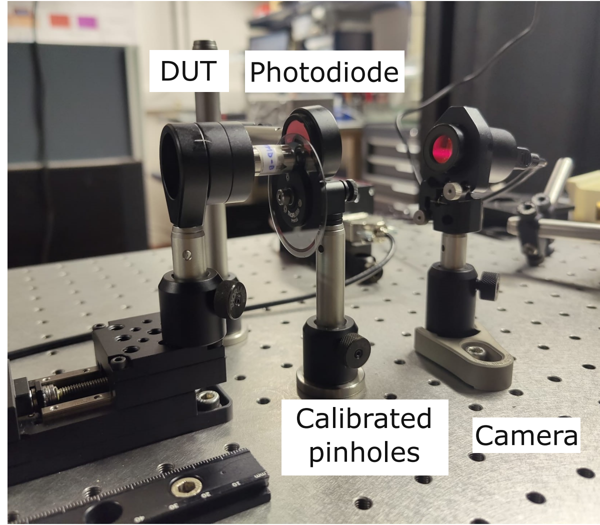

Figure 4.2: View of our setup - DUT: Device Under Test.

The test conducted with the setup described above entails measuring the transmission of the laser beam through calibrated pinholes positioned at the focal distance of the lenses under analysis. This procedure utilizes the previously mentioned calibrated pinhole wheel, where each pinhole diameter requires precise positioning to optimize the optical power captured by the laser power meter. The EE can be defined as the fraction of transmitted power through the aperture of a given pinhole with radius r_{ph}. It can be evaluated as [19]:

$$\mathrm{EE(r_{ph})} = \frac{\int_0^{2\pi} \mathrm{d}\varphi \int_0^{r_{ph}} I(r,\varphi) r \mathrm{d}r}{\int_0^{2\pi} \mathrm{d}\varphi \int_0^{\infty} I(r,\varphi) r \mathrm{d}r} \tag{4.1}$$

where $I(r, \varphi)$ is the intensity distribution of the laser beam on the pinhole plane (PSF) and the denominator of the eq. (4.1) can be evaluated assuming that the aperture of the largest available pinhole (radius 1 mm), when properly centered on the beam axis, transmits completely the laser beam.

Chapter 5

Conclusions and Outlook

The fabrication process of metalenses presents several challenges that demand careful analysis and the development of effective protocols to enhance the final outcome. In this section, I will summarize our current status, discuss some of the key challenges encountered during the fabrication process, and propose strategies to address them.
Since the DON group had no previous experience with titanium dioxide and amorphous silicon, I have carried out a technological development with both materials. Despite non-trivial challenge, notable progress has been made during my internship.
For the TiO_2 metalenses, we are now able to spin a thicker resist and perform a conformal deposition of amorphous titanium dioxide with the correct refractive index for the visible range through ALD. However, there are still some aspects to optimize. One of the remaining challenges in the fabrication of titanium dioxide metalenses is the inadequate development of the resist. To address this issue, a proposed strategy involves reducing the baking time for the first resist layer, which can help prevent material overheating and improve resist development. Additionally, exploring the use of more suitable developers for the resist might further optimize the resist development process. Should the problem persist and turn out to be unrelated to the development step, attention will be redirected to the Electron Beam Lithography (EBL) step. It is possible that our exposure dose is too low to fully expose all the resist and induce the necessary change in solubility. Therefore, conducting further dose tests with significantly higher doses might prove important to achieve complete resist exposure.
Regarding the fabrication of amorphous silicon metalenses, we have successfully achieved the correct pattern using PMMA resist and the appropriate dose. Additionally, we can completely remove the Ni-mask without affecting the silicon substrate, but the protocol still needs to be optimized. From the initial recipe of reactive ion etching, some progress has been made, but further improvements are necessary. This involves experimenting with varying gas ratios, adjusting pressure, and RF power settings to achieve more anisotropic and controlled etching. Furthermore, exploring other techniques such as ICP-RIE could offer opportunities to achieve more vertical and precise etching.
The experience and results obtained so far pave the way for future developments and improvements. Prof. Leo's group will continue the work initiated during this internship, focusing on the fabrication and characterization of linear metalenses. Regarding TiO_2 metalenses, one of the most promising applications is in intraocular lenses and contact lenses, within the framework of a European project. Metalenses based on optical metasurfaces can address various optical needs by minimizing spherical aberrations, improving multifocal

efficiency, correcting high-order aberrations, and introducing new strategies for reducing myopia progression. Additionally, wavefront engineering technology using metalenses is a powerful tool for developing innovative solutions for rare but severely debilitating conditions such as keratoconus, metamorphopsia, and age-related macular degeneration (AMD).

Bibliography

[1] R. C. Devlin, M. Khorasaninejad, W. T. Chen, J. Oh, and F. Capasso, "Broadband high-efficiency dielectric metasurfaces for the visible spectrum," *Proceedings of the National Academy of Sciences*, vol. 113, no. 38, pp. 10 473–10 478, Sep. 2016, ISSN: 1091-6490. DOI: 10.1073/pnas.1611740113. [Online]. Available: https://doi.org/10.1073/pnas.1611740113.

[2] H. Pahlevaninezhad, M. Khorasaninejad, Y.-W. Huang, *et al.*, "Nano-optic endoscope for high-resolution optical coherence tomography in vivo," *Nature Photonics*, vol. 12, no. 9, pp. 540–547, Jul. 2018, ISSN: 1749-4893. DOI: 10.1038/s41566-018-0224-2. [Online]. Available: https://www.nature.com/articles/s41566-018-0224-2.

[3] D. Visser, S. B. Basuvalingam, Y. Désières, and S. Anand, "Optical properties and fabrication of dielectric metasurfaces based on amorphous silicon nanodisk arrays," *Optics Express*, vol. 27, no. 4, p. 5353, Feb. 2019, ISSN: 1094-4087. DOI: 10.1364/oe.27.005353. [Online]. Available: https://opg.optica.org/oe/fulltext.cfm?uri=oe-27-4-5353&id=405055.

[4] M. Khorasaninejad and F. Capasso, "Metalenses: Versatile multifunctional photonic components," *Science*, vol. 358, no. 6367, Dec. 2017, ISSN: 1095-9203. DOI: 10.1126/science.aam8100. [Online]. Available: https://www.science.org/doi/10.1126/science.aam8100.

[5] C. Gigli, Q. Li, P. Chavel, G. Leo, M. L. Brongersma, and P. Lalanne, "Fundamental limitations of huygens' metasurfaces for optical beam shaping," *Laser & Photonics Reviews*, vol. 15, no. 8, p. 2 000 448, Jun. 2021, ISSN: 1863-8899. DOI: 10.1002/lpor.202000448. [Online]. Available: https://onlinelibrary.wiley.com/doi/abs/10.1002/lpor.202000448.

[6] J. Engelberg and U. Levy, "The advantages of metalenses over diffractive lenses," *Nature Communications*, vol. 11, no. 1, Apr. 2020, ISSN: 2041-1723. DOI: 10.1038/s41467-020-15972-9. [Online]. Available: https://www.nature.com/articles/s41467-020-15972-9.

[7] G.-Y. Lee, J. Sung, and B. Lee, "Metasurface optics for imaging applications," *MRS Bulletin*, vol. 45, no. 3, pp. 202–209, Mar. 2020, ISSN: 1938-1425. DOI: 10.1557/mrs.2020.64. [Online]. Available: https://link.springer.com/article/10.1557/mrs.2020.64.

[8] T. Hu, Q. Zhong, N. Li, *et al.*, "Cmos-compatible a-si metalenses on a 12-inch glass wafer for fingerprint imaging," *Nanophotonics*, vol. 9, no. 4, pp. 823–830, Feb. 2020, ISSN: 2192-8614. DOI: 10.1515/nanoph-2019-0470. [Online]. Available: https://www.degruyter.com/document/doi/10.1515/nanoph-2019-0470/html.

[9] W. Liu, D. Ma, Z. Li, *et al.*, "Aberration-corrected three-dimensional positioning with a single-shot metalens array," *Optica*, vol. 7, no. 12, p. 1706, Dec. 2020, ISSN: 2334-2536. DOI: 10.1364/optica.406039. [Online]. Available: https://opg.optica.org/optica/fulltext.cfm?uri=optica-7-12-1706&id=444154.

[10] M. O'Byrne, B. Kerzabi, M. Abbarchi, *et al.*, "Investigation of the anatase-to-rutile transition for TiO_2 solgel coatings with refractive index up to 2.7," *Thin Solid Films*, vol. 790, p. 140 193, Feb. 2024, ISSN: 0040-6090. DOI: 10.1016/j.tsf.2023.140193. [Online]. Available: https://www.sciencedirect.com/science/article/pii/S0040609023005266?via=ihub.

[11] Y.-W. Kim and D.-H. Kim, "Atomic layer deposition of TiO2 from tetrakis-dimethylamido-titanium and ozone," *Korean Journal of Chemical Engineering*, vol. 29, no. 7, pp. 969–973, Jun. 2012, ISSN: 1975-7220. DOI: 10.1007/s11814-012-0072-6. [Online]. Available: https://link.springer.com/article/10.1007/s11814-012-0072-6.

[12] InRedox, *Atomic Layer Deposition in Nanopores*, 2017. [Online]. Available: https://www.inredox.com/technology/atomic-layer-deposition/ (visited on 2024).

[13] Y. Wang, Q. Chen, W. Yang, *et al.*, "High-efficiency broadband achromatic metalens for near-IR biological imaging window," *Nature Communications*, vol. 12, no. 1, Sep. 2021, ISSN: 2041-1723. DOI: 10.1038/s41467-021-25797-9. [Online]. Available: https://www.nature.com/articles/s41467-021-25797-9.

[14] D. Yang, J. Wang, R. Li, Y. Ma, and L. Ma, "Extremely vertical sidewall trench etching on silicon substrate and modelling etching using artificial neural network," *Materials Research Express*, vol. 6, no. 12, p. 125 902, Nov. 2019, ISSN: 2053-1591. DOI: 10.1088/2053-1591/ab55b4. [Online]. Available: https://iopscience.iop.org/article/10.1088/2053-1591/ab55b4.

[15] P. Spinelli, "Light trapping in solar cells using resonant nanostructure," *Thesis,externally prepared, Universiteit van Amsterdam*, p. 145, 2013. [Online]. Available: https://hdl.handle.net/11245/1.400657.

[16] R. Legtenberg, H. Jansen, M. de Boer, and M. Elwenspoek, "Anisotropic reactive ion etching of silicon using $SF_6/O_2/CHF_3$ gas mixtures," *Journal of The Electrochemical Society*, vol. 142, no. 6, pp. 2020–2028, Jun. 1995, ISSN: 1945-7111. DOI: 10.1149/1.2044234. [Online]. Available: https://iopscience.iop.org/article/10.1149/1.2044234.

[17] J. Proust, A.-L. Fehrembach, F. Bedu, I. Ozerov, and N. Bonod, "Optimized 2D array of thin silicon pillars for efficient antireflective coatings in the visible spectrum," *Scientific Reports*, vol. 6, no. 1, Apr. 2016, ISSN: 2045-2322. DOI: 10.1038/srep24947. [Online]. Available: https://www.nature.com/articles/srep24947.

[18] Optikos. "Encircled energy and ensquared energy on LensCheck lens measurement systems." (2024), [Online]. Available: https://www.optikos.com/articles/encircled-energy-and-ensquared-energy-on-lenscheck-lens-measurement-systems (visited on 2024).

[19] M. Kalpana Devi, C. Srinivas, and T. Venkat Reddy, "Energy parameters of symmetrical optical system apodized with gaussian filter," *International Journal of Scientific Engineering and Research (IJSER)*, vol. 6, 6 Jun. 2018. [Online]. Available: https://www.ijser.in/archives/v6i6/IJSER172656.pdf.